Front. Optoelectron. 2013, 6(3): 261–269
DOI 10.1007/s12200-013-0340-z

RESEARCH ARTICLE

Hybrid surface plasmon modes in metal-clad Si/SiO_2 waveguide for compact integration

Xiaoliu ZUO, Zhijun SUN (✉)

Department of Physics, Xiamen University, Xiamen, Fujian 361005, China

Abstract This paper investigated characteristics of hybrid surface plasmon waveguiding modes in metal-clad Si/SiO_2 waveguide. Mode characteristics are shown to be highly dependent on structure dimensions and polarization states. By controlling the structure dimensions, a compromise between propagation loss and field confinement can be made for the waveguiding modes. Here, the waveguide had been particularly designed to have very low loss, in which power is mainly confined in the high-index Si-core region to propagate. This waveguide showed excellent bending, isolation and coupling properties that is suitable for high-density integrated photonic circuits.

Keywords waveguides, surface plasmon (SP), photonic integrated circuits, metal

1 Introduction

Hybrid integration of electronic and photonic circuits on a single chip has become a key route to develop faster and more capable device units for information processing [1]. But the size of the photonic section is usually much larger than that of the electronic parts, which will increase the cost (for large chip size but low-efficiency utilization of the area, and others) and affect the performance of the integrated systems. The major issue in miniaturization of integrated photonic circuits is to develop waveguides that can be integrated in high density. This has been a subject extensively studied in recent years both in fundamental level [2] and technological developments. Various novel waveguides are thus proposed, including photonic crystal (PC) waveguides [3], dielectric slot waveguides [4] and plasmonic waveguides [5]. Meanwhile, Si waveguides with conventional structures showed great potentials due to their large index contrast [6]; and they are also compatible with Si-based electronics in terms of both processing and hybrid integration. Nevertheless, the all-dielectric ones are in any case still subject to the diffraction limit, which eventually limits their application for compact waveguide circuits. The plasmonic waveguides are able to highly confine the light beyond the diffraction limit, but stronger confinement is usually accompanied with more absorption loss due to intrinsic properties of surface plasmons (SP). In the past few years, researchers come to be interested in hybrid SP modes that are based on introduction of low/high-index dielectric layers near the metal surfaces [7–12]. This configuration can highly confine the light in the low-index dielectric region; meanwhile its absorption loss is relatively lower. More recently, double low-index nano-slots waveguides based on such hybrid SP modes have been proposed [13–17], which can also highly confine the power in the low-index region showing very small mode area.

In our view, the current key problems in miniaturization of waveguide circuits are concentrated on compact waveguide bending and inter-waveguide isolation for high-density integration, instead of small transverse-dimensions or ultra-small mode area of the waveguides, as they have been already well acceptable being in the scale of wavelength or subwavelength. Of course, promising waveguides should also be low-lossy and feasible in building various functional components, e.g. couplers, resonators and switches. Additionally, fabrication of the waveguides are expected better compatible with current planar Si processing technologies for hybrid integration of electronics and photonics circuits on single Si chips.

Previously, we proposed a type of hybrid SP waveguide that was similar to the above mentioned double low-index nano-slots waveguides, but it was designed such that the power of light was mainly confined in the high-index core region instead of the low-index region to propagate [18]. Experimentally, we fabricated such a waveguide with a core region of triangular-like cross-section, and a low loss

Received April 28, 2013; accepted May 20, 2013

E-mail: sunzj@xmu.edu.cn

of 1.6 dB/mm at λ = 1550 nm was demonstrated [19]. In this work, we had comprehensive analysis on characteristics of the hybrid SP modes and their dependences on the structure dimensions and polarization states, as well as some initial investigations on relevant integration issues, such as waveguide bending, coupling and isolation.

2 Model and methods

Figure 1 shows a schematic illustration of the waveguide structure that is used in the numerical analyses. It consists of a silicon core region, surrounded by an oxide (SiO_2) layer and additionally coated with a metal (Ag) cladding layer. Such a structure is feasible to be fabricated on a silicon-on-insulator (SOI) substrate with current micro/nano-fabrication technologies. The oxide layer sandwiched between the Si-core and Ag-clad can be directly deposited using sputtering (or plasma-enhanced chemical vapor deposition) techniques, or partially grown by thermal oxidation. The oxide in the bottom region is the BOX layer of the SOI substrate, which is considered to be thick enough, such that the Si base is not considered in the schematic model for analysis. In all the calculations, vacuum wavelength of the light is set at 1550 nm, the permittivity of Ag is $-103.2 + 8.1i$, and the indices of Si and SiO_2 are assumed to be 3.5 and 1.5 respectively. As indicated in Fig. 1, w_1 and w_2 are the widths of the rectangular Si-core region and the oxide region on both sides of it; t_1 and t_2 are the thicknesses of the Si-core region and its top oxide layer; t_0 is the thickness of the oxide layer between the Si-core region and the bottom level of the Si/SiO_2 ridge, where the y-coordinate is zero. In the x-coordinate, $x = 0$ locates on the symmetric middle line of the Si-core. In all the calculations, thickness of the Ag clad (t_{Ag}) is 200 nm; and t_0 = 0.5 μm.

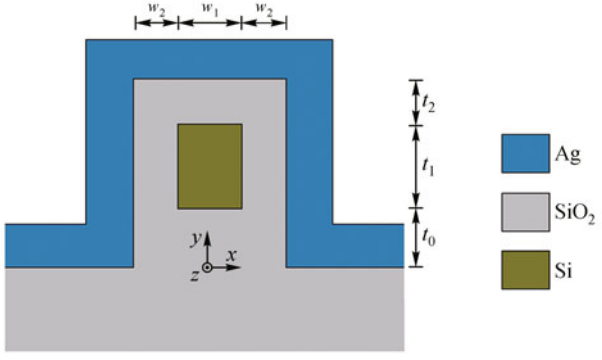

Fig. 1 Schematic cross-section of metal-clad Si/SiO_2 waveguide

In the numerical simulations, finite element method (FEM) was used to analyze the waveguide modes, which includes calculations of the waveguide mode indices (or mode effective indices), mode profiles and field distributions in the transverse cross sections. In analyses of the waveguide propagation properties, finite-difference time-domain (FDTD) method was used to calculate the waveguide bending loss, cross-talk between isolated neighboring waveguides, directional coupling length, and coupling efficiency between waveguides with and without the metal clad.

3 Results and discussion

3.1 Waveguide modes in different polarization states

Using FEM analysis, first two waveguide modes with the lowest-order are identified as shown in Fig. 2, which are strongly dependent on polarization states of the fields. Here we used "P_x-mode" and "P_y-mode" to label them. For the P_x-mode, the transverse electric field is dominant in the x-direction (i.e., the E_x field). For the P_y-mode, the transverse electric field is dominant in the y-direction (i.e., the E_y field). It is also shown that, for both types of modes, distributions of the magnetic fields H_x, H_y, and H_z are correspondingly similar to those of the electric fields E_y, E_x and E_z when a 90°-rotation of them is performed around the longitudinal z-axis, except that discontinuities appear at the Si/SiO_2 boundaries for the electric fields normal to the interfaces (e.g., the E_x-field for the P_x-mode and the E_y-field for the P_y-mode). As all the media are nonmagnetic, the magnetic fields show no discontinuities at the boundaries. We also examined the polarization-dependent modes with FDTD simulations, in which Gaussian sources are used to excite the propagating waves. It was confirmed that field distributions of the P_x- and P_y-modes in Fig. 2 can be exactly excited by setting the polarization of source field to be in the x- and y-directions respectively. It is noted that the thicknesses of the surrounding oxide layers (w_2, t_2) are relative large here in Fig. 2. As the dimensions (w_2, t_2) become extremely small (e.g., ~10 nm), distributions of the field appear quite differently, i.e., the electric field (E_x for P_x-mode, or E_y for P_y-mode) distributes mainly in the narrow oxide gap. But intrinsically they are of the same type modes as shown in Fig. 2; and there is only strong variation of the relative field magnitudes in the Si-core and the sandwiched SiO_2 regions for different structure dimensions. It is noted that, compared to conventional metal-clad optical waveguide [20] or metal-insulator-metal (MIM) SP waveguide, the metal-induced absorption loss is thus able to be highly reduced by modifying the field distributions in the high/low-index Si/SiO_2 regions, which results in the current hybrid SP modes.

3.2 Dependence of mode characteristics on structure dimensions

As an example, we calculated the complex effective indices (N_{eff}, or mode indices) of the P_x- and P_y-modes of

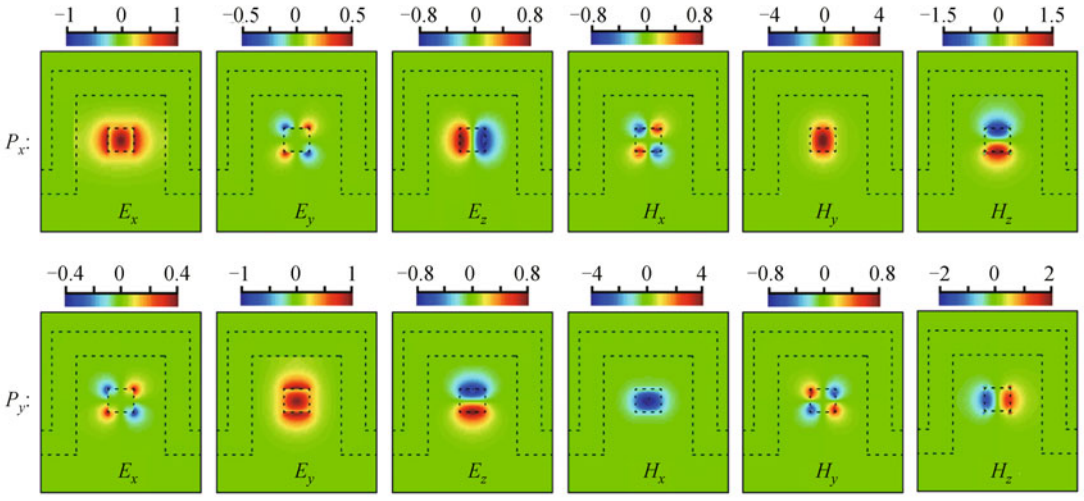

Fig. 2 Distributions of field components in transverse cross-sections for P_x- (top) and P_y-polarization (bottom) modes of a waveguide with dimensions $w_1 = t_1 = 300$ nm and $w_2 = t_2 = 400$ nm. Labels (E_x, E_y, E_z; H_x, H_y, H_z) in the images indicate the electric and magnetic field components projected in the directions of x-, y-, and z-axis as defined in Fig. 1. As the modes are non-transverse electromagnetic (EM) modes, all six components of the fields are demonstrated

the proposed waveguide with $w_1 = t_1 = 300$ nm, $w_2 = 400$ nm, and $t_2 = 600$ nm, and those that one of the dimensions in each individual is varied, which are shown in Fig. 3. Figure 3 shows that the effective indices have typical dependence on the structure dimensions. Considering the metal-induced loss only, the propagation length (L_p) of a waveguide mode is related to the imaginary effective index, $L_p = \lambda/[4\pi \cdot \mathrm{Im}(N_{eff})]$, which is also indicated for reference. It is noted that the minimum dimensions of w_1 and t_1 shown in Fig. 3 are 200 nm, because there are cutoffs below it for both the P_x- and P_y-modes. For too small values of w_1 and t_1, transverse distributions of the fields are not to be confined in the Si-core or sandwiched oxide layer regions, but abnormal showing maximum field magnitude at the sharp corners of the Ag-clad, i.e., at $x = \pm(w_2 + w_1/2)$, $y = 0$. This is not the mode of our interest.

In Figs. 3(a) and 3(c), it is shown that, as both w_2 and t_2 are relatively large, the real effective indices of the P_x- and P_y-modes are nearly the same at $w_1 = t_1 = 300$ nm. But, when there is a large discrepancy of w_1 and t_1 ($w_1/t_1 > 1$ or < 1), one of the modes (P_x- or P_y-mode) has a larger real effective index, showing polarization birefringence. This is also observed in Figs. 3(b) and 3(d) that, since $w_1 = t_1$, real effective indices of the P_x- and P_y-modes become very close as w_2 and t_2 are increased to be large enough (e.g. > 300 nm), approaching a constant value. It tells that, with increase of the oxide layer thicknesses (w_2, t_2), effects of the metal clad are weakened, and the modes will be more like those of a conventional dielectric waveguide. On the contrary, when the oxide layer thicknesses (w_2, t_2) are very small (e.g. less than ~200 nm), the effective indices of the modes change dramatically with respect to the variation of w_2 and t_2, and the polarization birefringence become very strong. This implies a distinct transition of the mode characteristics that we will see in the following analyses based on transverse distributions of the field and power. From the subplots for imaginary effective indices in Fig. 3, it is shown that the waveguiding loss decreases dramatically with increase of any of the structure dimensions w_1, w_2, t_1 and t_2, which also corresponds to a weakening of the field confinement.

Figures 4(a) and 4(b) show transverse distributions of the E_x-field and power flow S_z for the P_x-mode of the waveguide analyzed in Fig. 3(b) when the side oxide layers are extremely narrow ($w_2 = 20$ nm) or wide ($w_2 = 400$ nm). It is clearly observed that, for $w_2 = 20$ nm in Fig. 4(a), the field and power locate dominantly in the narrow oxide layer, which is similar to that reported in literatures [13–15]. For the large w_2 of 400 nm in Fig. 4(b), the maximum E_x-field locates inside and at the side edges of the Si-core region, while the power is highly confined in the core region. Similarly, as shown in Figs. 4(c) and 4(d) for the P_y-mode, it is observed that, for a thin top oxide layer $t_2 = 20$ nm (Fig. 4(c)), the maximum field and power locate in the thin top oxide layer; but for a thick top oxide layer $t_2 = 400$ nm (Fig. 4(d)), the maximum E_y-field locate inside and at the up/bottom-side edges of the Si-core region; and the power distributes dominantly in the core region. It should be pointed out that, despite of the differences in field and power distributions for the waveguides with largely discrepant oxide layer thicknesses in Figs. 4(a) and 4(b) or in Figs. 4(c) and 4(d), they are still attributed to the same type and order of modes. Their field distribution functions in different regions of the waveguides follow the same expression forms, while the functional parameters are different.

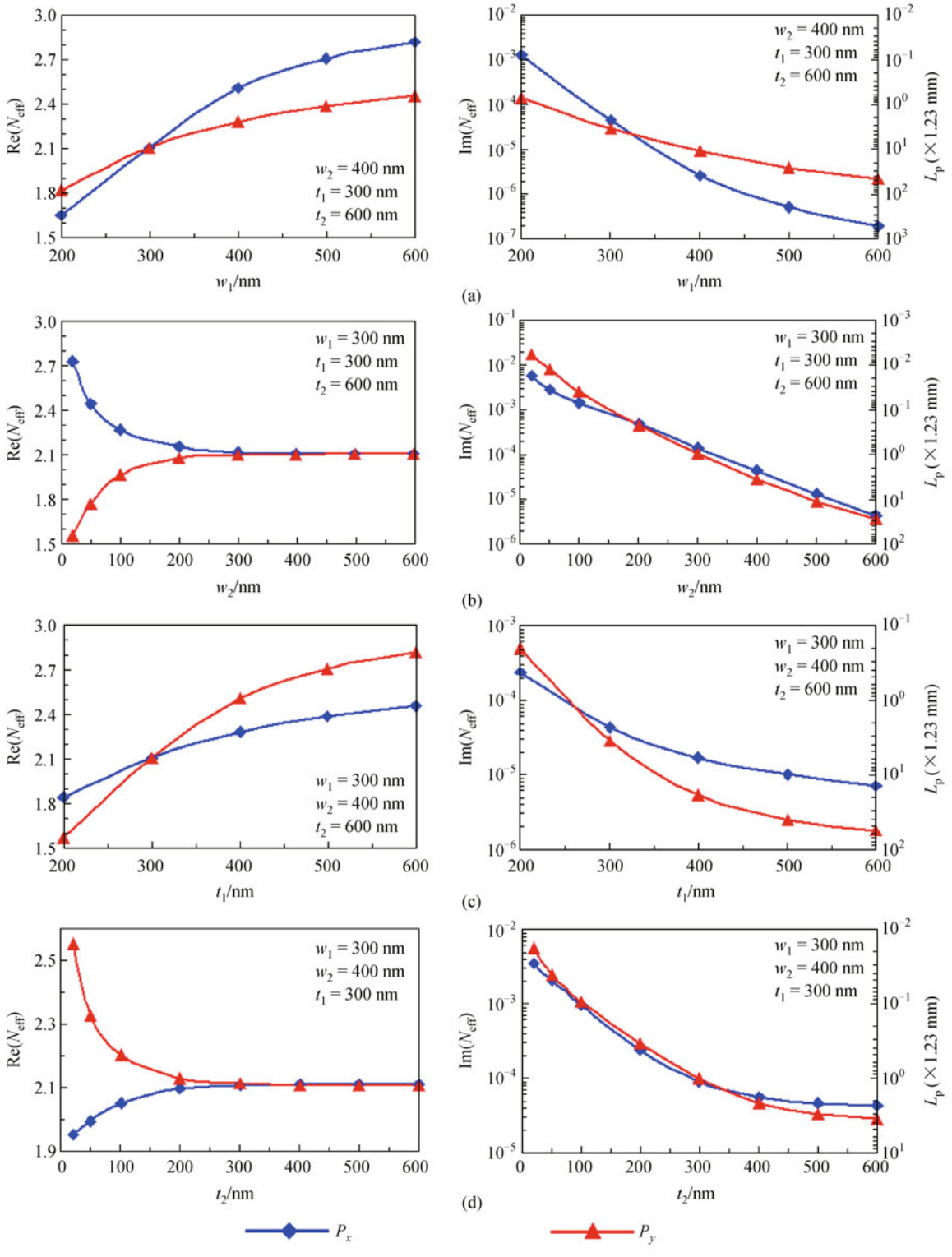

Fig. 3 Dependences of real and imaginary parts of the mode index (N_{eff}) of a waveguide ($w_1 = t_1 = 300$ nm, $w_2 = 400$ nm, and $t_2 = 600$ nm) on its structure dimensions. The propagation lengths (L_p) at $\lambda = 1550$ nm are also indicated, corresponding to the imaginary part

Fundamentally, the above waveguiding mode is a hybridization of the "*SP mode*" at the metal/dielectric interfaces and the "*optical mode*" in a conventional low/high-index dielectric waveguide. Thus, dependence of the mode characteristics on the structure dimensions is intrinsically a matter of compromise between the field

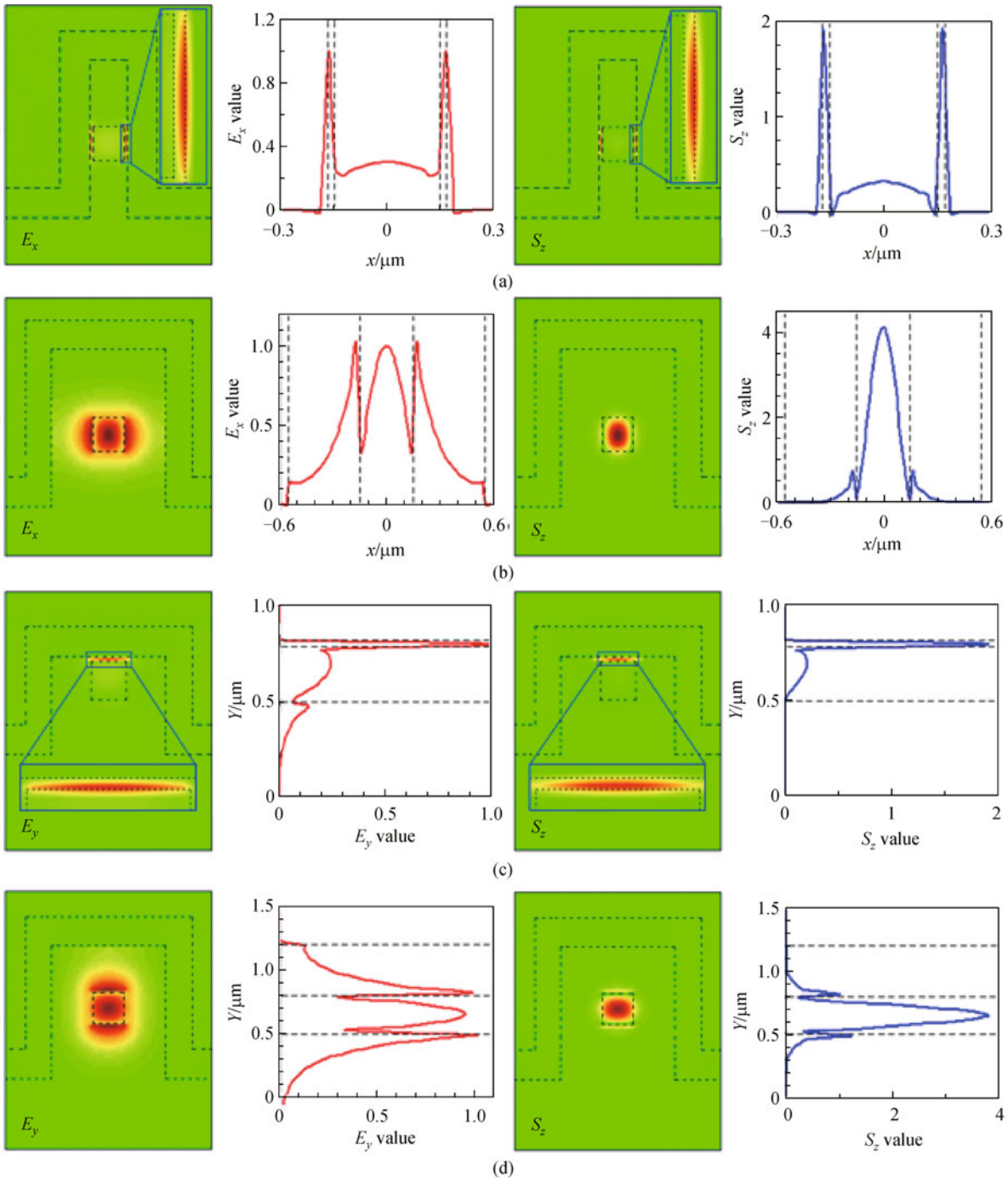

Fig. 4 (a, b) Transverse distributions of E_x-field and power flow S_z for P_x-mode of waveguides ($w_1 = t_1 = 300$ nm, $t_2 = 600$ nm) with very narrow or wide side oxide layers ($w_2 = 20$ nm in (a), $w_2 = 400$ nm in (b)); (c, d) transverse distributions of E_y-field and power flow S_z for P_y-mode of waveguides ($w_1 = t_1 = 300$ nm, $w_2 = 400$ nm) with a very thin or thick top oxide layer ($t_2 = 20$ nm in (c), $t_2 = 400$ nm in (d)). On right side of each color image is an x- or y-scan of the field or S_z across the core center

confinement and the propagation loss. When the SP-component is dominant, confinement is stronger in the low-index oxide region, but the loss is higher; when the optical-component is dominant, confinement is weaker distributing mainly in the high-index Si region, and the loss is relatively much lower. Eventually, functional purpose in application of the waveguide is a key consideration in specific design. Particularly, for high-density waveguide routing in integrated photonic circuits, ultra-high field confinement in waveguide may not be necessary; thus a lower-loss optical-component dominant hybrid SP mode is more of our interest, which requires relatively wider/

thicker oxide layers. For example, the propagation lengths of such a waveguide with $w_1 = t_1 = 300$ nm, $w_2 = 400$ nm, and $t_2 = 600$ nm, are approximately 3 mm for both the P_x- and P_y-modes, corresponding to a loss of about 1.5 dB/mm.

3.3 Configurations and performances of waveguide bending, isolation and coupling

Here, we studied the transmission and mode properties of a 90° waveguide bend as schematically shown in Fig. 5(a), which has a circularly rounded corner. The bend radius (R) is defined referring to the middle line in the waveguide core. For a waveguide with $w_1 = 300$ nm, $w_2 = t_1 = 400$ nm, and $t_0 = t_2 = 500$ nm, we calculated bending loss for various radius. The results are shown in Fig. 5(b), compared to those of the waveguides just without the metal clad. Generally, the bending losses decrease with increase of the radius, and are rather low even as the bend radius is in the order of wavelength or further below. And compared to the waveguides without the metal clad, the metal clad apparently results in higher loss for the P_x-mode; but for the P_y-mode, the bending loss is slightly lower for the metal-clad one. This is because, for the P_x-mode, field of the SP-component distributes at the flanking side metal surfaces, which is heavily involved in confinement of the power at the outside boundary of the corner. Usually, stronger SP field induces more absorption loss. For the P_y-mode, field of the SP-component distributes at the inner top metal surface, which is weakly modified at the corner; thus its absorption loss is almost invariant. But the side metal clad prohibits any radiation loss at the corner that the non-metal-clad one cannot avoid; the overall bending loss is thus lower for the P_y-mode of the metal-clad waveguide, particularly prominent for very small radius. Figures 5(c) and 5(d) demonstrate simulated distributions of the instantaneous magnitude of the power flow ($|S|$) and fields (H_y for the P_x-mode and E_y for the P_y-mode). It is observed that the power is more spread to the outside inner boundary of the metal at the corner for the P_x-mode, which brings more absorption loss than that of the P_y-mode. From transverse distributions of the power flow

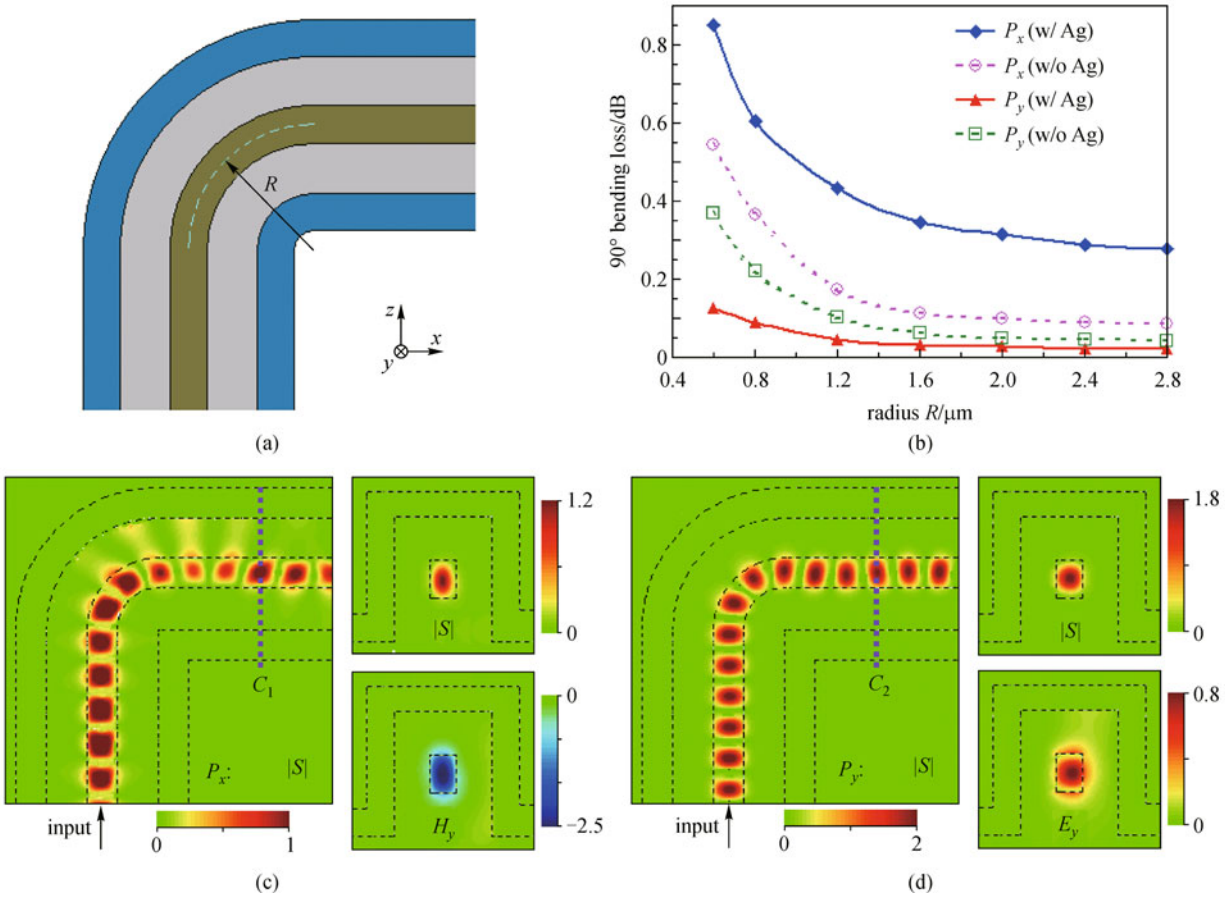

Fig. 5 (a) Schematic illustration of 90° circular-round waveguide bending; (b) dependence of bending loss on bend radius (R) for waveguides with and without metal Ag clad in P_x- or P_y-mode. Here $w_1 = 300$ nm, $w_2 = t_1 = 400$ nm, and $t_0 = t_2 = 500$ nm; (c) and (d) show longitudinal cross-sectional ($y = 0.7$ μm) view of the power flow for P_x- and P_y-mode waves propagating through a bend with $R = 0.6$ μm. The small panels on the right side of (c) and (d) show transverse cross-section distributions of power flow $|S|$ and H_y (or E_y) field after propagating through the bend, at the positions indicated with dash-lines C_1 and C_2

magnitude and field at the cross-sections C_1 and C_2, we can see that, after transmission through the bending corner, the power is still well confined mainly within the Si-core region and the waveguiding modes are maintained, which can be verified by comparing the fields with those in Fig. 2. Note that cross-section distributions of the x-components and z-components of the magnetic and electric fields are interchanged after wave propagating through the 90° bend due to definition of the rectangular coordinate, and hence we show here only y-components of the fields.

In Figs. 6(a)–6(c), configurations of some waveguide structures are demonstrated inter-waveguide isolation, directional coupling, and integration with conventional Si-based waveguides. For directional coupling, Si-cores of two neighboring waveguides share the same metal clad in the coupling region. For hybrid integrate with conventional Si waveguides, it only need to deposit an additional metal layer on top of the dielectric waveguides in the region where compact arrangement of waveguides is necessary. A SiO_2 layer should be deposited (or produced by selective thermal oxidation) before metal coating if it is originally a bare Si waveguide. Using FDTD simulations, we calculated that, for two neighboring waveguides with $w_1 = 300$ nm, $w_2 = t_1 = 400$ nm, $t_0 = t_2 = 500$ nm, and their interspacing of a few hundred nanometers (e.g. $d_i = 200$–600 nm) as shown in Fig. 6(a), the cross-talk is well below -30 dB, a level usually considered to be negligible. When the interspacing and t_0 are further increased, the cross-talk decreases dramatically.

For directional waveguide coupling in Fig. 6(b), we calculated the dependence of the coupling length (L_c) on the interspacing between waveguide cores (d_c), as shown in Fig. 6(d). The calculations using FDTD method is straightforward by directly considering the field distributions. In the other approach for comparison, the finite element method is used first to determined the mode indices of the even ($N_{e,eff}$) and odd ($N_{o,eff}$) supermodes in the coupled system; then the coupling length is calculated using the formula [21]:

$$L_c = \pi/(\beta_o - \beta_e),$$

$$\beta_o = (2\pi/\lambda) \cdot N_{o,eff},$$

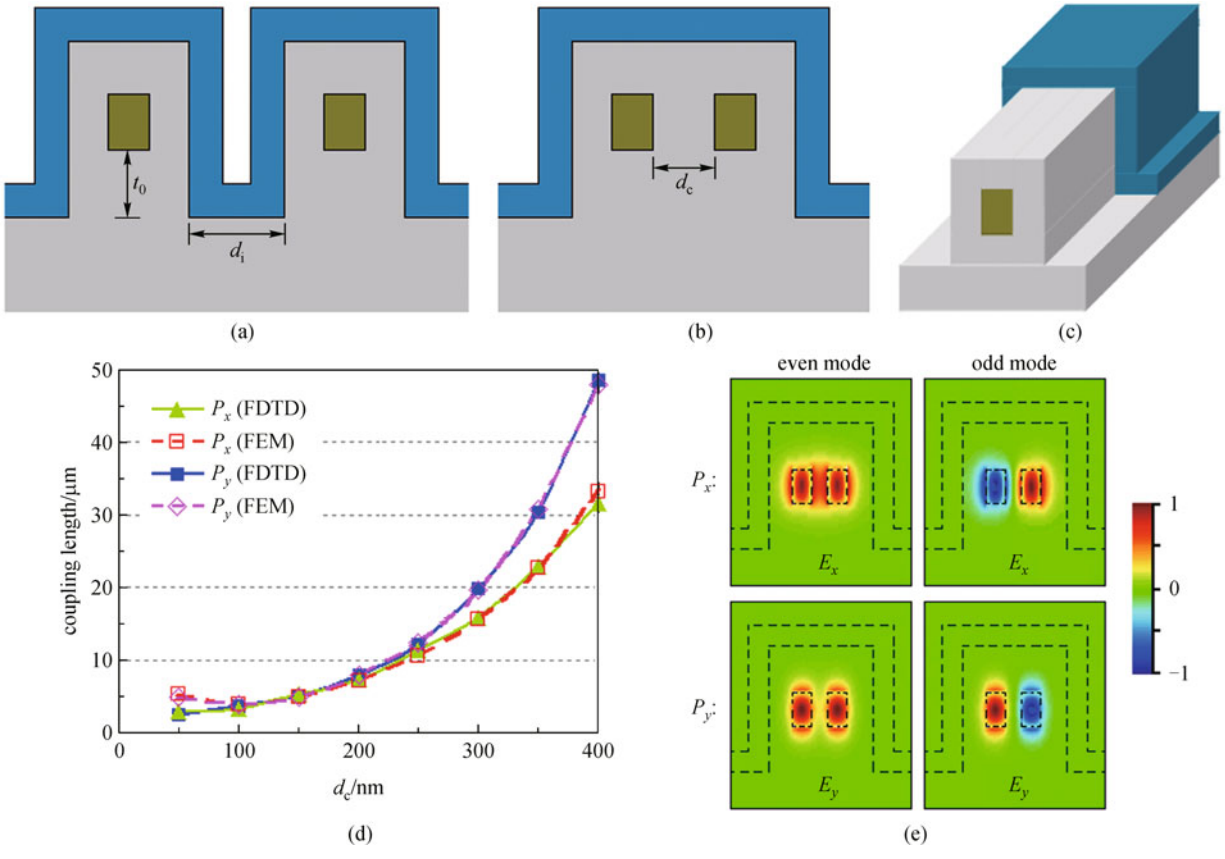

Fig. 6 Schematic illustrations of waveguide structure for inter-waveguide isolation (a), directional coupling (b) and connection with its non-metal-clad Si/SiO_2 waveguide (c); (d) dependence of coupling length on the interspacing between neighboring waveguide cores for directional coupling, calculated with FDTD and FEM methods. The waveguides have $w_1 = 300$ nm, $w_2 = t_1 = 400$ nm, and $t_0 = t_2 = 500$ nm; (e) field distributions of even (left column) and odd (right column) supermodes of coupled waveguides ($d_c = 300$ nm) fore corresponding P_x- (upper row) and P_y-modes (lower row) of individual ones

$$\beta_e = (2\pi/\lambda) \cdot N_{e,eff}.$$

In Fig. 6(e), transverse distributions of the E_x- and E_y-fields of the supermodes are demonstrated for coupling of the P_x- and P_y-polarization modes, in which the fields are distributed either symmetrically (for the even mode) or antisymmetrically (for the odd mode) with respect to the symmetry plane of the structure. The results determined with the two methods show great consistency in Fig. 6(d), except at very small interspacings, e.g., $d_c < 100$ nm. Deviation of the FEM-results from those of FDTD for very small d_c is related to arising of the gap mode between high-index dielectric regions in the FEM calculations. It is additionally observed that the coupling length is weakly dependent on the polarization states of the modes when the core-interspacing is relatively small (e.g., $d_c < 250$ nm); but for a larger d_c, a large discrepancy is apparent. It is worth mentioning that dependence of the coupling length on the core-interspacing is confirmed to be well exponential.

For integrated connection of the waveguides with and without the metal cladding layer in Fig. 6(c), we studied the coupling at the junction region. It was shown that the coupling efficiency is strongly dependent on the dimensions of w_1, w_2, t_1 and t_2 when they are relatively small; but for larger dimensions of them, the coupling efficiency is very high, e.g., well above 99.99% for $w_1 = 300$ nm, $w_2 = t_1 = 400$ nm, and $t_0 = t_2 = 500$ nm, according to the simulation results.

4 Conclusions

In this paper, we investigated the waveguide modes in metal-coated Si/SiO_2 ridge waveguide that can be fabricated on SOI substrates. The modes generally have hybrid characteristics of SP modes and optical modes in all-dielectric Si waveguides. These waveguide modes are dependent on structure dimensions and polarization states. The weight of both components in the hybrid modes can be adjusted, which determines the level of field confinement and propagation loss that are usually in contradiction. Especially, for low-loss waveguiding, dimensions of the Si and SiO_2 regions in the waveguide should be relatively larger, but they can be still in a sub-micrometer scale. Such waveguides show excellent bending, isolation and coupling properties, and can be directly integrated with non-metal-clad Si/SiO_2 waveguides with low coupling loss. It was suggested that such hybrid SP waveguides is enough good to be adopted only in particular regions of an integrated photonic circuit, where they can present more advantageous performances in sharp waveguide bending, isolation and enhancement of light-matter interaction processes in nonlinear and active waveguide components.

Acknowledgements This work was supported in part by the National Natural Science Foundation of China (Grant No. 61275063), the National Key Scientific Program (No. 2012CB933503), the Natural Science Foundation of Fujian Province of China (No. 2011J06002) and the Fundamental Research Funds for the Central Universities (No. 2012121009).

References

1. Pavesi L, Guillot G, eds. Optical Interconnects: The Silicon Approach. Berlin: Springer, 2006
2. Wehrspohn R B, Kitzerow H S, Busch K, eds. Nanophotonic Materials: Photonic Crystals, Plasmonics, and Metamaterials. Weinheim: WILEY-VCH Verlag GmbH & Co KGaA, 2007
3. Joannopoulos J D, Meade R D, Winn J N. Photonic Crystals: Molding the Flow of Light. 2nd ed. Princeton: Princeton University Press, 2008
4. Almeida V R, Xu Q, Barrios C A, Lipson M. Guiding and confining light in void nanostructure. Optics Letters, 2004, 29(11): 1209–1211
5. Bozhevolnyi S I. Plasmonic Nanoguides and Circuits. Singapore: Pan Stanford Publishing Pte Ltd, 2009
6. Vlasov Y A, McNab S J. Losses in single-mode silicon-on-insulator strip waveguides and bends. Optics Express, 2004, 12(8): 1622–1631
7. Oulton R F, Sorger V J, Genov D A, Pile D F P, Zhang X. A hybrid plasmonic waveguide for subwavelength confinement and long-range propagation. Nature Photonics, 2008, 2(8): 496–500
8. Dai D, He S. A silicon-based hybrid plasmonic waveguide with a metal cap for a nano-scale light confinement. Optics Express, 2009, 17(19): 16646–16653
9. Avrutsky I, Soref R, Buchwald W. Sub-wavelength plasmonic modes in a conductor-gap-dielectric system with a nanoscale gap. Optics Express, 2010, 18(1): 348–363
10. Wu M, Han Z, Van V. Conductor-gap-silicon plasmonic waveguides and passive components at subwavelength scale. Optics Express, 2010, 18(11): 11728–11736
11. Goykhman I, Desiatov B, Levy U. Experimental demonstration of locally oxidized hybrid silicon-plasmonic waveguide. Applied Physics Letters, 2010, 97(14): 141106
12. Kim J T, Ju J J, Park S, Kim M S, Park S K, Shin S Y. Hybrid plasmonic waveguide for low-loss lightwave guiding. Optics Express, 2010, 18(3): 2808–2813
13. Dai D, He S. Low-loss hybrid plasmonic waveguide with double low-index nano-slots. Optics Express, 2010, 18(17): 17958–17966
14. Zhu S, Liow T Y, Lo G Q, Kwong D L. Fully complementary metal-oxide-semiconductor compatible nanoplasmonic slot waveguides for silicon electronic photonic integrated circuits. Applied Physics Letters, 2011, 98(2): 021107
15. Kim J T, Choi S E. Hybric plasmonic slot waveguides with sidewall slope. IEEE Photonics Technology Letters, 2012, 24(3): 170–172
16. Kwon M S. Metal-insulator-silicon-insulator-metal waveguides compatible with standard CMOS technology. Optics Express, 2011, 19(9): 8379–8393
17. Kim J T. CMOS-compatible hybrid plasmonic slot waveguide for on-chip photonic circuits. IEEE Photonics Technology Letters, 2011, 23(20): 1481–1483

18. Sun Z, Zuo X, Li J, Liu B. Hybridized low-loss plasmonic-optical waveguides for ultra-compact integration. In: Proceedings of the Society for Photo-Instrumentation Engineers, 2010, 7874: 78470O
19. Zuo X, Sun Z. Low-loss plasmonic hybrid optical ridge waveguide on silicon-on-insulator substrate. Optics Letters, 2011, 36(15): 2946–2948
20. Takano T, Hamasaki J. Propagating modes of a metal-clad-dielectric-slab waveguide for integrated optics. IEEE Journal of Quantum Electronics, 1972, 8(2): 206–212
21. Dai D, Shi Y, He S. Comparative study of the integration density for passive linear planar light-wave circuits based on three different kinds of nanophotonic waveguide. Applied Optics, 2007, 46(7): 1126–1131